Ocean Engineering 148 (2018) 588–601

Contents lists available at ScienceDirect

Ocean Engineering

journal homepage: www.elsevier.com/locate/oceaneng

# Drained monotonic and cyclic capacity of a dynamically installed plate anchor in sand

S.H. Chow [a,*], C.D. O'Loughlin [b], C. Gaudin [b], J.T. Lieng [c]

[a] Centre for Offshore Foundation Systems, 35 Stirling Highway, Crawley, WA 6009, Australia
[b] Centre for Offshore Foundation Systems, Crawley, WA 6009, Australia
[c] GeoProbing Technology, P.O. Box 1227 Pirsenteret, 7462 Trondheim, Norway

ARTICLE INFO

*Keywords:*
Anchors
sands
Offshore engineering
Renewable energy
capacity

ABSTRACT

The emergence of commercial offshore floating renewable energy devices that are expected to be deployed in large integrated arrays in relatively shallow water requires anchor types that are suited to sandy seabeds. This paper considers centrifuge test data that quantify the capacity of a novel dynamically installed plate anchor in sand under drained monotonic and cyclic loading. The monotonic tests investigated the role of the eccentricity of the load attachment point from the plate, the mooring line load inclination at the seabed and the plate embedment depth, whereas the cyclic tests examined the capacity mobilisation due to both regular and irregular drained cyclic loading for a fixed embedment depth and seabed load inclination. The test data indicate that an optimal anchor design would employ a load attachment point that is eccentric from the plate by at least 0.6 times the plate height, and that the anchor provides higher capacity when the seabed load inclination is horizontal (catenary mooring) than when it is vertical (vertical taut mooring). The centrifuge data show that drained cyclic loading does not degrade anchor capacity, and may be beneficial provided the cyclic loading involves a history of lower level cyclic loading that densifies the sand.

## 1. Introduction

Offshore renewable energy devices, including wind turbines, wave and tidal energy converters, offer significant potential to move towards clean, renewable energy. Floating wave energy convertor and wind turbines are maintained on station using mooring lines that terminate at anchors located on or embedded in the seabed. Knappett et al. (2015), Diaz et al. (2016) and Gaudin et al. (2017) review existing anchor technology in the context of the technical requirements and economic constraints associated with offshore floating renewable energy. These studies note that plate anchors are attractive due to their high holding capacity yet low size and weight, although difficulties in installing plate anchors in the sand dominated seabeds that floating energy devices are likely to be located may constrain their use. Plate anchors may be installed by drag embedment, although adequate penetration of drag anchors in sand is notoriously difficult and challenging to predict (Neubecker and Randolph, 1996; Heurlin et al., 2015; O'Loughlin et al., 2017). Other anchor types, such as driven piles may be used, although they are less efficient, and installation requirements and durations are considerable. This has the potential to seriously impact the economics of emerging marine renewable energy technologies, which will be deployed in large integrated arrays requiring a large number of accurately positioned anchors.

An alternative solution could be dynamically installed anchors, which require minimal installation time and can be deployed without the need for dedicated ancillary equipment such as pile hammers. Dynamically installed anchors are installed by allowing them to free-fall through the water column, such that the combination of their self-weight and the kinetic energy gained through free-fall embed them into the seabed. Various anchor designs have been proposed for deep water soft sediments (e.g. Lieng et al., 2000; Medeiros Jr. 2002; Shelton, 2007; O'Loughlin et al., 2014) and have been used or considered for offshore oil and gas floating facilities. Current dynamically installed anchors are generally perceived to be less suitable for sand due to the dilatant behaviour of sand and concerns regarding embedment potential. However, alternative dynamically installed anchor designs may achieve higher penetrations in sand, and prove to be a viable anchoring solution for granular seabed deposits (e.g. Gerkus et al., 2016).

* Corresponding author.
*E-mail addresses:* shiaohuey.chow@uwa.edu.au (S.H. Chow), conleth.oloughlin@uwa.edu.au (C.D. O'Loughlin), christophe.gaudin@uwa.edu.au (C. Gaudin), jon.lieng@geoprobing.com (J.T. Lieng).

https://doi.org/10.1016/j.oceaneng.2017.11.051
Received 19 September 2017; Received in revised form 13 November 2017; Accepted 26 November 2017
Available online 6 December 2017

This paper considers one such dynamically installed anchor concept that has been designed primarily for sand, although may also prove to be feasible in other seabed sediments. The anchor and the installation process is conceptually shown in Fig. 1. The anchor adopts a thin 'blade-like' design which contrasts with the majority of existing dynamically installed anchor designs that typically utilise solid cylindrical shafts with conical or ellipsoidal tips (O'Loughlin et al., 2004). The anchor features a plate at its lower end that is attached to an upper removable follower that provides the additional mass to increase penetration potential. In cross-section the plate is comprised of two thin blades that project from a central core, and taper from a maximum width at the top of the plate to zero width at the bottom of the plate. Two additional fins at the trailing end of the upper follower (Fig. 1) are included to improve hydrodynamic stability during freefall in water. Following embedment, the follower is retrieved to the installation vessel for re-use in the next installation, leaving the plate anchor vertically embedded in the seabed.

The embedment potential of the anchor has been demonstrated through centrifuge tests in loose and dense silica sand (Chow et al., 2017). Anchor tip embedments were in the range 0.9–2.2 times the plate height in these centrifuge tests, and were strongly dependent on impact velocity, follower mass and sand density. This suggests that deeper anchor embedment could be achieved by geometrically optimising the follower. Subsequent centrifuge studies investigated the monotonic and cyclic capacity of the anchor in saturated dense silica sand to quantify the capacity potential of the anchor. The results from these studies are considered in this paper.

## 2. Centrifuge tests

### 2.1. Soil properties and sample preparation

The centrifuge tests were conducted in medium dense sand samples that were prepared using a commercially available fine sub-angular silica sand with properties as listed in Table 1. Seven sand samples were prepared at 1*g* in centrifuge sample containers with internal dimensions of 650 × 390 × 325 mm (length × width × depth) by air pluviation to give final sample heights of approximately 200 mm. Each sample was vacuum-levelled to create a level surface and then saturated with water from the base of the container. About 40 mm of free water was maintained above the sand surface during the centrifuge testing. The relative density was $D_r$ = 66 ± 3% (saturated densities, $\rho_{sat}$ = 2034–2043 kg/cm$^3$), with the exception of one slightly looser sample for which $D_r$ = 53% ($\rho_{sat}$ = 2017 kg/cm$^3$). Each sample was spun to the testing acceleration of 50 g and two cone penetrometer tests (CPTs) were conducted to characterise the samples. The cone penetrometer tests were performed using a model cone penetrometer with a diameter of 10 mm penetrated at a velocity, $v$ = 1 mm/s such that the response is expected to be drained (Silva and Bolton, 2004). As shown in Fig. 2, the cone tip resistance, $q_c$, increases with depth in all samples, which reflects the increasing vertical effective stress with depth. Variations in $q_c$ between samples are consistent with the measured range in $D_r$, and indicate that the profile of strength and density is relatively consistent across the seven samples.

**Table 1**
Properties of silica sand used in this study.

| Property | Value |
|---|---|
| Specific gravity, $G_s$ | 2.67 |
| Particle size, $d_{10}$, $d_{50}$, $d_{60}$ | 0.12, 0.18, 0.19 mm |
| Coefficient of uniformity, $C_u$ | 1.67 |
| Coefficient of curvature, $C_c$ | 1.02 |
| Minimum dry density, $\rho_{min}$ | 1497 kg/m$^3$ |
| Maximum dry density, $\rho_{max}$ | 1774 kg/m$^3$ |
| Critical state friction angle, $\phi'_{cs}$ | 31.6° (triaxial) |

### 2.2. Model anchors and mooring line

Four model anchors (A1, A2, A3, A4) were manufactured for the centrifuge tests as shown in Fig. 3. Each model anchor was wire-cut (electrical discharge machining) from a single block of stainless steel, followed by precision machining to achieve the detail around the anchor padeye and the taper on the plate. The models are at a 1:50 reduced scale and maintain the same material density as the field scale anchor, such that the centrifuge scaling laws (Garnier et al., 2007) apply. These imply that a practically sized full-scale anchor would have a plate height of 2.4 m, a follower length of 7.25 m (with a mass of 5134 kg) and an anchor mass of between 1290 and 1960 kg (depending on the anchor), although variations on this are to be expected based on the mooring requirements.

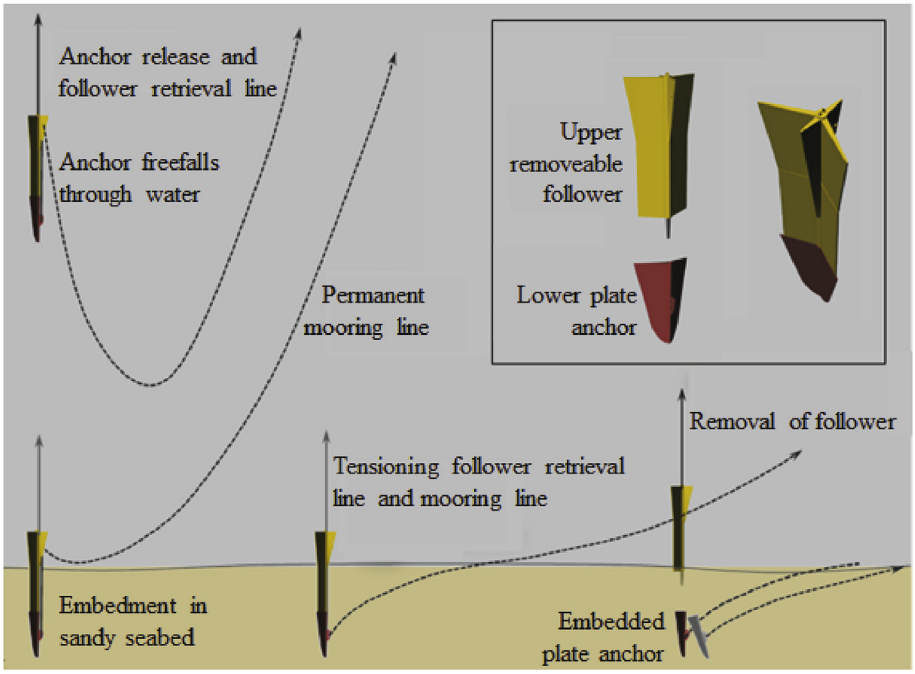


**Fig. 1.** Dynamically installed anchor concept.

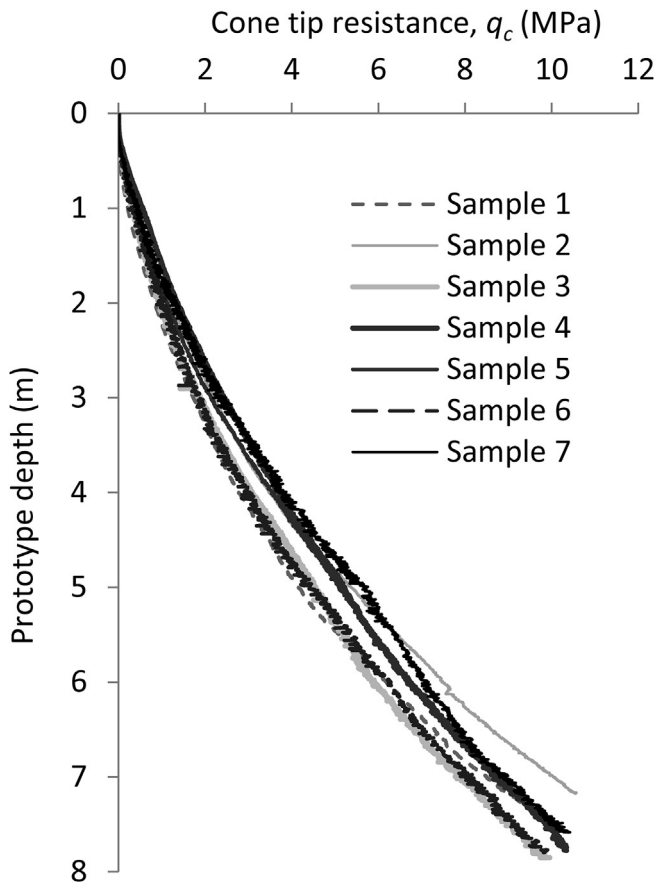


**Fig. 2.** Cone tip resistance profiles.

The mooring line was modelled using 1 mm diameter stainless steel wire rated to a minimum breaking load of 1.1 kN (Fig. 3d).

Anchor A1 (Fig. 3) reflects the original design as shown in Fig. 1 and has a plate mass, $m = 10.32$ g, plate width, $W = 36$ mm, plate length, $L_p = 48$ mm and plate thickness, $t = 1.52$ mm at the central core, thinning out to t = 0.1 mm at the edge. The anchor padeye in the original design – and hence in anchor A1 – is located at an eccentricity normal to the plate, $e_n = 7$ mm (padeye eccentricity ratio, $e_n/L_p = 0.15$).

Initial tests using the A1 anchor revealed that when loaded through a catenary mooring the anchor moved vertically upwards with little or no rotation, which limited the capacity to frictional resistance along the surface area of the plate. This behaviour was attributed to the low padeye eccentricity, which limited the moment loading on the plate and hence the rotation necessary to mobilise bearing resistance. Similar behaviour has been observed for plate anchors in clay (e.g. O'Loughlin et al., 2006; Tian et al., 2015). This prompted a reconsideration of the anchor design, and led to fabrication of three additional anchors with padeye eccentricities, $e_n = 14$, 29 and 48 (as shown in Fig. 3a), which correspond to padeye eccentricity ratios, $e_n/L_p = 0.3$, 0.6 and 1. These designs were expected to encourage anchor rotation (or keying), allowing bearing resistance to be mobilised more readily and higher anchor capacity to be generated. All four anchors share a common follower (Fig. 3c), which had the wall thickness and profile of the anchors and was 145 mm in length. As this series of centrifuge tests involved jacked-in rather than dynamic installation, the follower was only used to penetrate the plate anchor to the required embedment depth.

As testing advanced it became apparent that continuous measurement of anchor rotation would benefit the interpretation. For this reason anchor A4 was instrumented with a dual-axis micro-electro mechanical system (MEMS) accelerometer (Analog Devices ADXL278). The ADXL278 accelerometer has a measurement range of ±70 *g* and ±35 *g* in its two measurement axes. It was located in an epoxy resin-filled void in the padeye of the anchor (see Fig. 3d) such that the ±70 *g* measurement axis was parallel to the centripetal acceleration vector in the centrifuge (and normal to the plate), making the accelerometer suited to these experiments conducted at 50 g and involving moderate anchor rotations.

Anchor rotation can be determined from the ratio of the two accelerometer measurements:

$$\alpha = \tan^{-1}\left(A_y/A_x\right) \quad (1)$$

where $A_x$ is the measured acceleration in the x-axis (parallel to the plate) and $A_y$ is the measured acceleration in the y-axis (normal to the plate). The accuracy of this measurement technique in a centrifuge environment is influenced by changes in anchor depth, as the acceleration level varies with radius. However, the change in accelerometer output is ±0.03 g for every millimeter change in anchor depth (model scale) at 50*g*, which would result in an error in the interpreted rotation (using Equation (1)) that is only ±0.06° for every millimeter change in anchor depth. As shown later in the paper (Fig. 11), anchor rotation established using Equation (2) was within 1–2° of direct measurements made after testing.

### 2.3. Experimental arrangement and procedures

The centrifuge tests were carried out at an acceleration of 50 *g* using the 1.8 m radius fixed beam centrifuge located at the University of Western Australia. The experimental arrangement is shown in Fig. 4, with notation for anchor embedment depth, anchor displacements, load inclination and anchor rotation shown in Fig. 5. Each centrifuge test involved first installing the model anchor vertically at 1*g* to the required penetration depth using the follower that was connected to the vertical axis of an electrically driven actuator. The model anchor was jacked-in at 1*g* rather than dynamically installed to ensure consistent embedment depths and hence identical initial stress conditions between tests. More details on the dynamic installation and embedment potential of the anchor are reported in Chow et al. (2017).

After anchor installation at 1*g* the centrifuge was spun up to 50*g* (with the follower and anchor position maintained using Actuator 1; see Fig. 4) and the follower removed before loading the anchor. The rational for removing the follower at 50*g* was to counter the tendency for the plate anchor to displace upwards with the follower as observed in initial tests in which the follower was extracted at 1*g*. The anchor was loaded with the mooring line either at a load inclination at the mudline, $\theta_m = 0°$ or $\theta_m = 90°$, representing a catenary or vertical taut-leg mooring respectively. The experimental arrangement was different for vertical (taut-leg) and catenary loading as shown in Fig. 4. For tests involving a catenary mooring ($\theta_m = 0°$), the mooring line was connected to a second actuator by way of a pulley located at the mudline directly beneath the vertical axis of the second actuator, such that the mooring line was maintained horizontal and along the mudline during loading (see Fig. 4a). For the vertical taut-leg mooring tests ($\theta_m = 90°$) the actuator used to install the anchor and retrieve the follower was also used to load the anchor as shown in Fig. 4b.

Anchor capacity was measured using a cylindrical load cell (6 mm in diameter and 25 mm in length) with a measurement range of 1 kN. This load cell was located in series with the mooring line at a position that ensured it remained above the mudline as the anchor was loaded. Displacement of the mooring line was measured by the encoder on the motor of the vertical axis of the actuator used to load the anchor.

The experimental programme involved both monotonic and cyclic loading. Monotonic loading was performed at an actuator velocity, $v = 1$ mm/s, such that the response is expected to be drained (for this sand). Cyclic loading was performed in load control using both irregular and regular loading at a frequency of 0.5 Hz. This value was selected to achieve a balance between high quality load control and moderate test durations, noting that this relatively low frequency will generate the targeted drained response in this sand. Each cyclic test commenced with

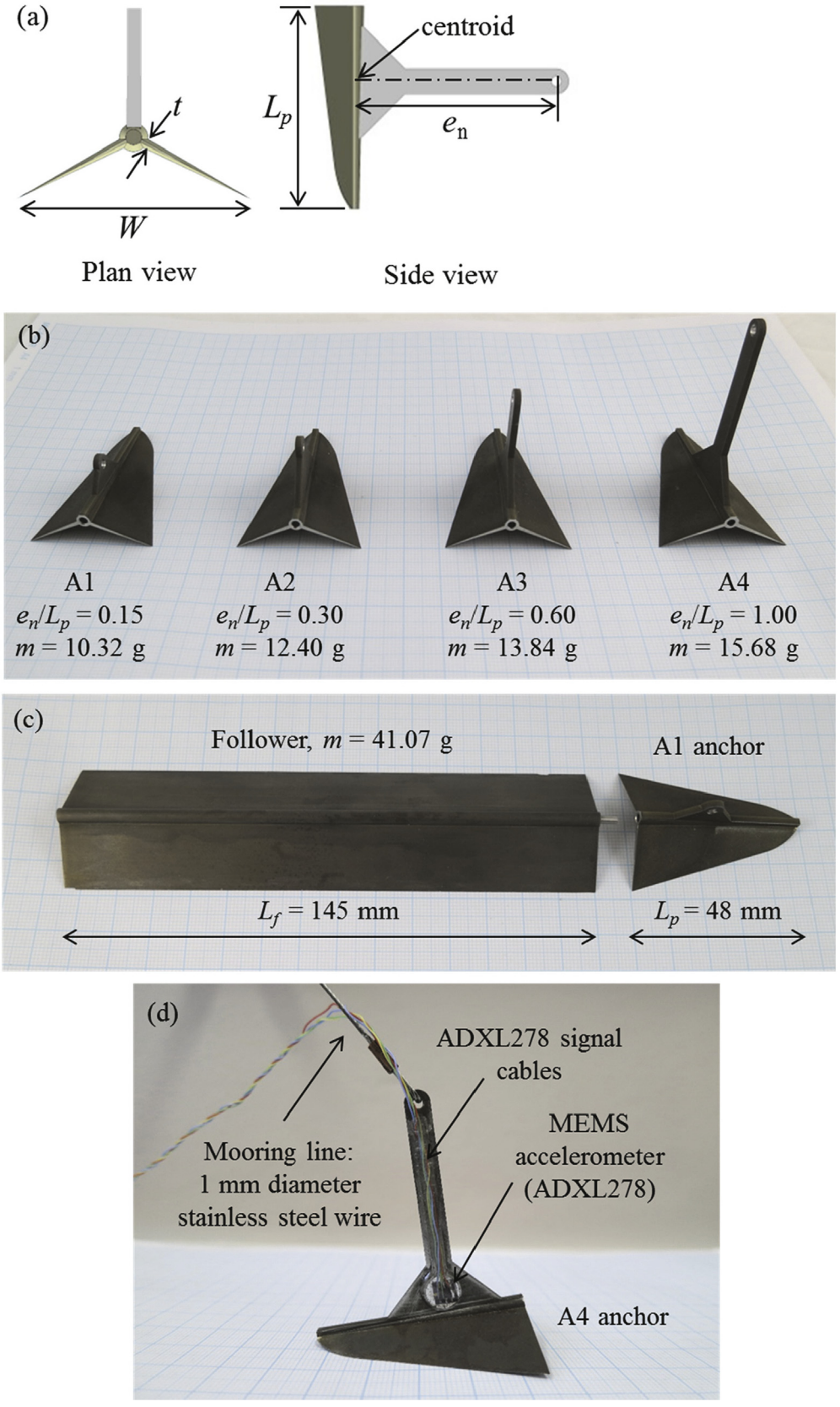


**Fig. 3.** Reduced scale anchor models: (a) schematic and notation; (b) plate anchors with different padeye eccentricities; (c) removable follower used to install each plate anchor; (d) anchor A4 instrumented with a MEMS accelerometer.

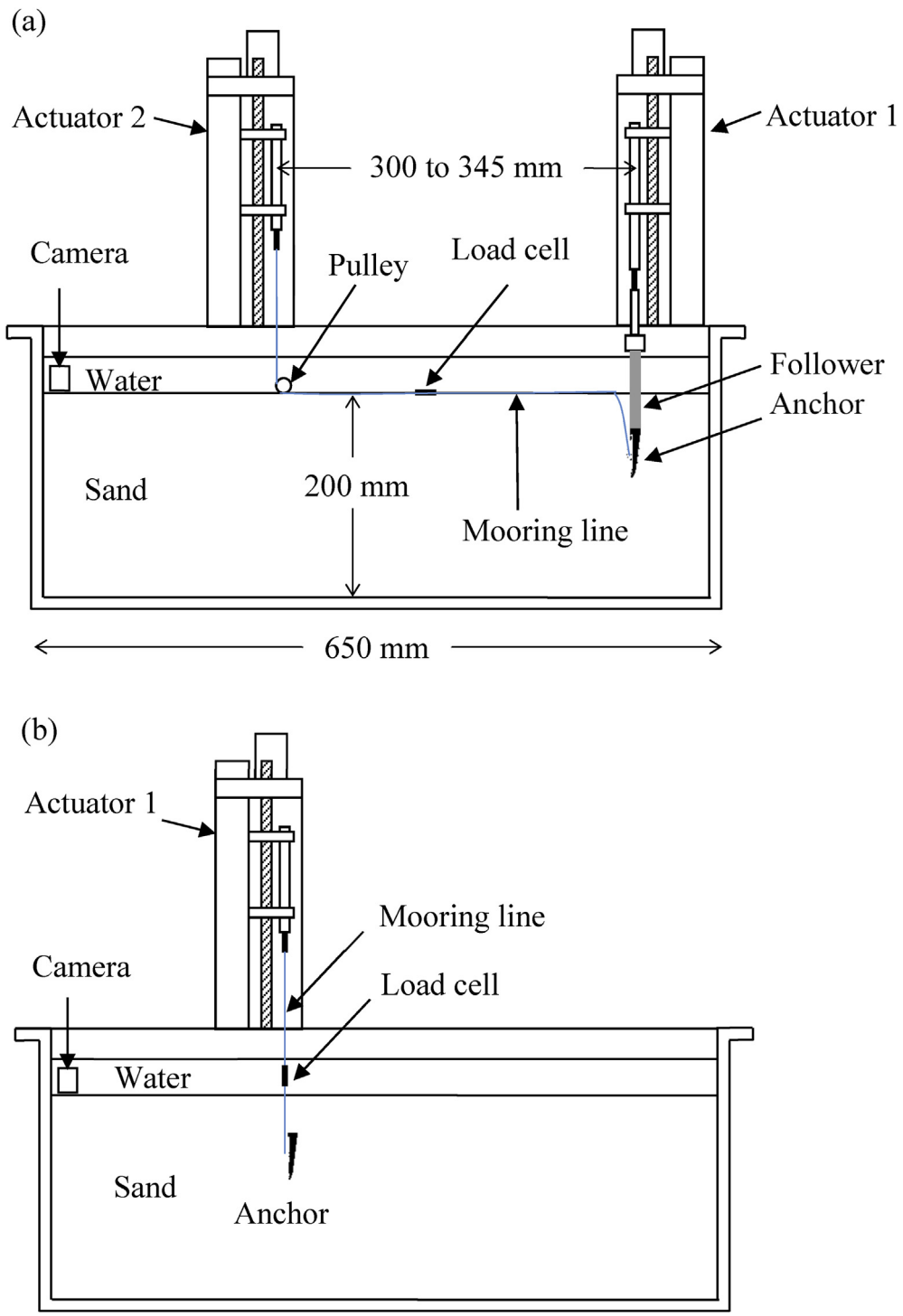


**Fig. 4.** Centrifuge test configuration: (a) anchor installation and loading through a catenary mooring ($\theta_m = 0°$); and (b) loading through a vertical taut-leg mooring ($\theta_m = 90°$).

an initial displacement controlled 'pre-load' stage at $v = 1$ mm/s to a cyclic load ratio, CLR $= F/F_u = 0.7$ (where $F$ is the imposed cyclic load and $F_u$ is the anchor capacity measured in the equivalent monotonic test), before starting the cyclic loading sequence. A post-cyclic loading monotonic test was conducted in tests where the anchor did not fail during cyclic loading. The monotonic tests were generally continued to beyond the ultimate anchor capacity, although in a number of tests the loading was stopped at or before the ultimate capacity to allow for a post-test visual assessment of the orientation and position of the anchor and its mooring line. In these instances, the anchor was left in the sample until completion of the tests, after which a longitudinal side wall of the sample container was removed and the sand excavated to expose the anchor and mooring line, allowing for measurement of the vertical and horizontal anchor displacement, the anchor inclination and the mooring line inclination at the padeye. In all other instances the anchor was recovered from the sample at 1 g for reuse in a subsequent test.

## 3. Test programme

The centrifuge test programme comprises 29 monontonic tests and 5 cyclic tests as summarised in Table 2. The monotonic tests consider variations in padeye eccentricity ratio ($e_n/L_p = 0.15, 0.3, 0.6, 1$), anchor

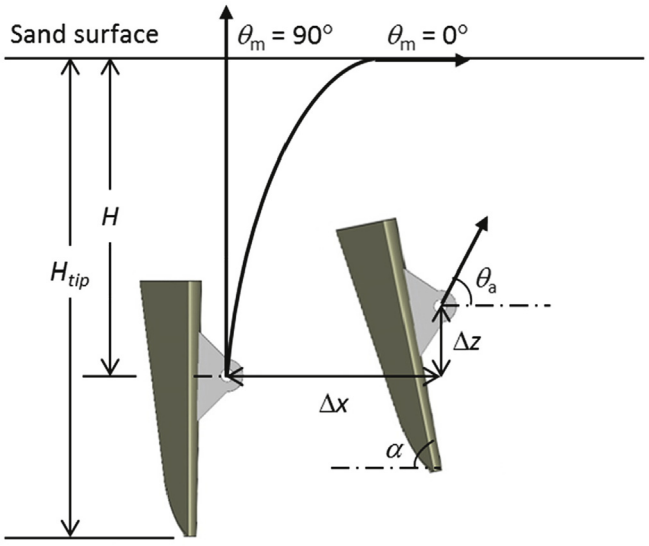


**Fig. 5.** Notation for embedments, displacements and inclinations.

embedment ratio ($H_{tip}/L_p$ = 2, 3) and load inclination ($\theta_m$ = 0, 90°). Although the cyclic tests considered only $e_n/L_p$ = 1, $H_{tip}/L_p$ = 2 and $\theta_m = 0°$, both regular and irregular cyclic loading were investigated, with different magnitudes of peak cyclic load to examine anchor performance when the cyclic loading included load magnitudes lower and higher than the monotonic capacity.

The tests are identified as LnIex, where 'L' denotes the type of loading and is either 'M' for monotonic loading, 'RC' for regular cyclic loading or 'IC' for irregular cyclic loading; 'n' is the anchor embedment ratio equal to 2 or 3 for $H_{tip}/L_p = 2$ and 3 respectively; 'I' denotes the load inclination at the mudline and is either 'C' for a catenary mooring ($\theta_m = 0°$) or 'V' for a taut-leg (vertical) mooring ($\theta_m$ = 90°); 'e' is the padeye eccentricity ratio normal to the anchor that is either 0.15, 0.3, 0.6 or 1 for $e_n/L_p$ = 0.15, 0.3, 0.6 and 1 respectively; 'x' is an alphabetic character denoting the test recurrence ('a' for the first test, 'b for the second test etc.). For instance, M2C0.15b refers to the second occurrence of a monotonic test involving $\theta_m = 0°$, $H_{tip}/L_p = 2$ and $e_n/L_p = 0.15$. For the two irregular cyclic loading tests in Table 2, the test name is appended with the peak CLR, either 1 or 1.5.

Table 2 also indicates if the tests involved a post-test visual assessment of the anchor and mooring line orientation and position – these were generally conducted either before, at or after the ultimate anchor capacity, as detailed in Table 2. Examination of Table 2 reveals that when tests were repeated, the results were consistent, with measurements varying typically by less than 10%.

Results from the monotonic tests are summarised in prototype scale or dimensionless form in Table 2 and include the ultimate capacity, $F_u$, and the corresponding normalised mooring line displacement, $\delta_u/L_p$, anchor rotation, $\alpha_u$, and the dimensionless anchor capacity factor, $N_\gamma$, determined as

$$N_\gamma = \frac{F_u}{\gamma' H A_p} \quad (2)$$

where $\gamma'$ is the effective unit weight of the sand, $A_p$ is the projected area of the anchor plate and $H$ is the initial depth to the anchor padeye (coincident with the initial depth to the centroid of the anchor). It is worth noting that Eq. (2) is expected to provide a conservative estimate of $N_\gamma$, as the depth to the centroid, $H$, will become progressively shallower during

**Table 2**
Centrifuge test programme and results (prototype scale).

| Test Series | | Anchor | $e_n/L_p$ | $H_{tip}/L_p$ | $H/L_p$ | $\theta_m$ (°) | $F_u$ (kN) | $\delta_u/L_p$ | $N_\gamma$ | $\alpha_u$ (°) | Observation[a] |
|---|---|---|---|---|---|---|---|---|---|---|---|
| Sample 1 | M3C1a | A4 | 1 | 3 | 2.375 | 0 | 2165.72 | 1.97 | 13.7 | | |
| ($\rho_{sat}$ = 2039 kg/cm$^3$) | M3C1b | A4 | 1 | 3 | 2.375 | 0 | 2050.46 | 2.22 | 12.9 | | After $F_u$ |
| | M3V1a | A4 | 1 | 3 | 2.375 | 90 | 1067.59 | 1.44 | 6.8 | | |
| | M3V1b | A4 | 1 | 3 | 2.375 | 90 | 1024.87 | 1.31 | 6.5 | | |
| Sample 2 | M3V0.15a | A1 | 0.15 | 3 | 2.375 | 90 | 335.86 | 0.59 | 2.3 | | |
| ($\rho_{sat}$ = 2038 kg/cm$^3$) | M3C0.15a | A1 | 0.15 | 3 | 2.375 | 0 | 1032.99 | 2.05 | 6.9 | | |
| | M3C0.15b | A1 | 0.15 | 3 | 2.375 | 0 | 998.64 | 1.82 | 6.7 | 90 | At $F_u$ |
| | M3C1c | A4 | 1 | 3 | 2.375 | 0 | 1914.54 | 1.65 | 13.6 | 74 | At $F_u$ |
| Sample 3 | M3C1d | A4 | 1 | 3 | 2.375 | 0 | – | – | – | | Before $F_u$ |
| ($\rho_{sat}$ = 2039 kg/cm$^3$) | M3C1e | A4 | 1 | 3 | 2.375 | 0 | 2084.37 | 1.97 | 13.2 | | |
| | M3C1f | A4 | 1 | 3 | 2.375 | 0 | 2012.38 | 1.71 | 12.8 | | |
| | M3C0.6a | A3 | 0.6 | 3 | 2.375 | 0 | 1956.50 | 1.73 | 12.4 | | |
| | M3C0.3a | A2 | 0.3 | 3 | 2.375 | 0 | 1740.75 | 1.69 | 11.0 | | |
| | M3C0.3b | A2 | 0.3 | 3 | 2.375 | 0 | 1659.38 | 1.65 | 10.5 | 82 | At $F_u$ |
| Sample 4 | M2C1a | A4 | 1 | 2 | 1.375 | 0 | 751.70 | 0.71 | 8.7 | | |
| ($\rho_{sat}$ = 2038 kg/cm$^3$) | M3C0.6b | A3 | 0.6 | 3 | 2.375 | 0 | 2040.96 | 1.70 | 13.0 | 79 | At $F_u$ |
| | M2C0.15a | A1 | 0.15 | 2 | 1.375 | 0 | 454.77 | 0.70 | 5.3 | | |
| | M2C1b | A4 | 1 | 2 | 1.375 | 0 | – | – | – | | Before $F_u$ |
| | M2C0.15b | A1 | 0.15 | 2 | 1.375 | 0 | 411.32 | 0.73 | 5.3 | | After $F_u$ |
| Sample 5 | M2C0.15c[b] | A1 | 0.15 | 2 | 1.375 | 0 | 508.70 | 0.63 | 5.9 | | After $F_u$ |
| ($\rho_{sat}$ = 2043 kg/cm$^3$) | M2C1b | A4 | 1 | 2 | 1.375 | 0 | 779.96 | 0.91 | 9.0 | | |
| | RC2C1a | A4 | 1 | 2 | 1.375 | 0 | 968.11 | 0.96 | 11.2 | | |
| | RC2C1b | A4 | 1 | 2 | 1.375 | 0 | 1037.39 | 0.98 | 12.0 | | |
| | RC2C1c | A4 | 1 | 2 | 1.375 | 0 | – | – | – | | Before $F_u$ |
| Sample 6 | M2C0.3a | A2 | 0.3 | 2 | 1.375 | 0 | 537.44 | 0.47 | 6.4 | | |
| ($\rho_{sat}$ = 2017 kg/cm$^3$) | M2C0.3b | A2 | 0.3 | 2 | 1.375 | 0 | 527.58 | 0.86 | 6.3 | | After $F_u$ |
| | M2C0.6a | A3 | 0.6 | 2 | 1.375 | 0 | 691.43 | 0.92 | 8.2 | | After $F_u$ |
| | M2C1c | A4 | 1 | 2 | 1.375 | 0 | 721.21 | 0.94 | 8.6 | 81.9 | |
| | IC2C1a1.5 | A4 | 1 | 2 | 1.375 | 0 | 863.43 | 0.92 | 10.2 | 82.1 | |
| | IC2C1a1 | A4 | 1 | 2 | 1.375 | 0 | 1029.96 | 0.88 | 12.3 | 82.9 | |
| Sample 7 | M3C0.15c | A1 | 0.15 | 3 | 2.375 | 0 | 919.79 | 1.56 | 6.2 | | |
| ($\rho_{sat}$ = 2034 kg/cm$^3$) | M2V0.15a | A1 | 0.15 | 2 | 1.375 | 90 | 93.58 | 0.10 | 1.1 | | After $F_u$ |
| | M2V1a | A4 | 1 | 2 | 1.375 | 90 | 225.12 | 1.34 | 2.6 | 13.7 | |
| | M3C1g | A4 | 1 | 3 | 2.375 | 0 | 1923.36 | 2.06 | 13.0 | 75.6 | After $F_u$ |

[a] Post-test anchor and mooring line visual assessment made before (~0.7 $F_u$), at ($F_u$) and after (~0.7 $F_u$) the ultimate capacity.
[b] Follower left-in-place during loading.

loading (as discussed later).

## 4. Results: monotonic capacity

### 4.1. Behaviour at low padeye eccentricity

The centrifuge modelling initially considered only anchor A1, which most closely replicates the original anchor design shown in Fig. 1. These tests considered both catenary and taut-leg mooring ($\theta_m = 0°$ and 90°) at two different embedment ratios ($H_{tip}/L_p = 2$ and 3). The anchor capacity response during the taut vertical mooring tests (i.e. Tests M2V0.15a and M3V0.15a) with the anchor embedded at $H_{tip}/L_p = 2$ and 3 are shown in Fig. 6a. The capacity mobilisation response for each test is similar, with an initial stiff response towards the ultimate capacity, followed by a rapid reduction in capacity as the plate displaces through the soil. Anchor capacity is evidently higher for the more deeply embedded anchor; $F_u = 94$ kN at $H_{tip}/L_p = 2$ and $F_u = 336$ kN at $H_{tip}/L_p = 3$, a 3.6 fold increase. The kinematic response of the anchor is evident from a post-test image of the exposed anchor in Test M2V0.15a, which was loaded beyond the ultimate capacity until the capacity reduced to about $0.7F_u$. The image is provided in Fig. 6b and shows that the anchor displaced vertically with minimal rotation ($\alpha = 87°$), such that anchor capacity is dominated by frictional resistance at the anchor-soil interfaces.

Anchor capacity improves for the same anchor ($e_n/L_p = 0.15$) when loaded under a catenary mooring ($\theta_m = 0°$). As shown in Fig. 7a, the ultimate anchor capacity in tests M2C0.15a and M3C0.15c are $F_u = 455$ kN at $H_{tip}/L_p = 2$ and 920 kN at $H_{tip}/L_p = 3$, which is 4.8 and 2.7 times higher than the respective ultimate anchor capacities under vertical loading. The capacity mobilisation response on Fig. 7a is different from that observed under vertical loading, with an initial soft response that becomes stiffer with increasing mooring line displacement and as the capacity approaches the peak value. The mooring line displacement at the peak capacity is higher for the more deeply embedded anchor, which

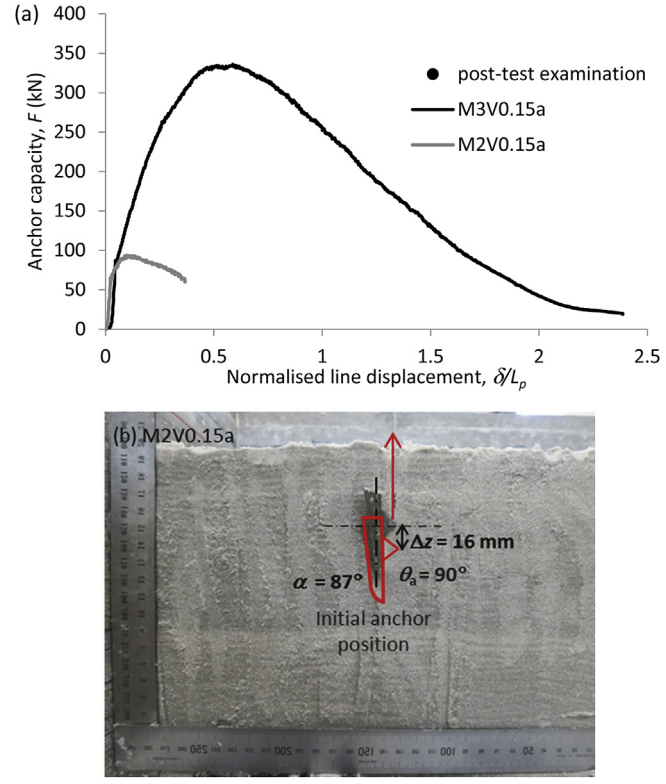


**Fig. 6.** (a) Capacity mobilisation for A1 anchor ($e_n/L_p = 0.15$) under taut (vertical) loading ($\theta_m = 90°$, $H_{tip}/L_p = 2$ and 3); (b) post-test visual examination of the anchor after loading to beyond the ultimate capacity (Test M2V0.15a).

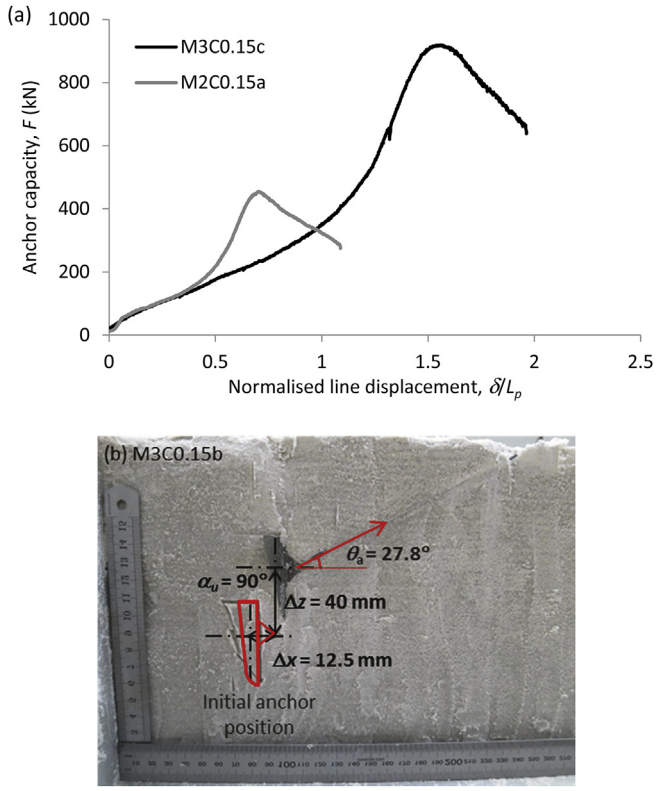


**Fig. 7.** Capacity mobilisation for A1 anchor ($e_n/L_p = 0.15$) loaded through a catenary mooring ($\theta_m = 0°$, $H_{tip}/L_p = 2$ and 3); (b) post-test visual examination of the anchor and mooring line at the ultimate capacity (test M3C0.15b).

reflects the higher amount of line displacement that is required to form the inverse catenary when the anchor padeye is deeper. Fig. 7b shows the position and orientation of the anchor and mooring line in a repeat test at $H_{tip}/L_p = 3$ (Test M3C0.15b), where the loading was stopped immediately after a peak capacity was observed ($F_u = 999$ kN). Although the anchor did not rotate ($\alpha_u = 90°$), the mooring line cut through the sand to form an inclination at the anchor padeye, $\theta_a = 27.8°$, such that the anchor displaced both laterally and vertically ($\Delta x/L_p = 0.26$, $\Delta z/L_p = 0.83$) and a component of resistance was mobilised in bearing. The movement of the mooring line through the soil is the likely reason for the initial soft response on Fig. 7a, as the stiffness due to vertical translation of the anchor (due to a vertical mooring line) is much higher (see Fig. 6a). This is explored further in Fig. 8, which compares the tests at $H_{tip}/L_p = 2$ with $\theta_m = 0°$ and 90° (i.e. as shown on Figs. 6a and 7a) with a further test (Test M2C0.15c), also at $H_{tip}/L_p = 2$ and with $\theta_m = 0°$, but in which the follower was held in position (using Actuator 1, see Fig. 4a) whilst the anchor was loaded (using Actuator 2, see Fig. 4a). This was maintained until the follower was observed to displace horizontally, at which point loading was temporarily paused to extract the follower. This approach restricted displacement and potential rotation of the anchor, permitting an observation of the response due to mooring line cutting alone. Fig. 8 shows that the initial response in the two tests with $\theta_m = 0°$ are consistent to about 100 kN, but then diverge, with the test with the follower in place continuing along a much stiffer response. This divergence indicates that in Test M2C0.15a (with no follower in place) the capacity response is initially due to mooring line cutting (to $F \approx 100$ kN) but then involves a combination of plate mobilisation and mooring line cutting.

This first set of tests highlights the importance of considering the coupled response of the anchor and its embedded mooring line in assessing the overall capacity. For a given anchor embedment, the highest potential anchor capacity is when the load is normal to the anchor. For an initially vertical anchor and mooring line, this requires a combination of anchor rotation and cutting of the mooring line through

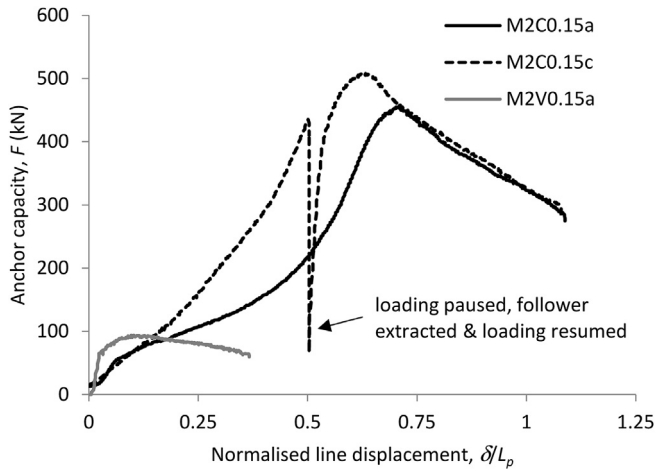


**Fig. 8.** Capacity mobilisation response with follower in-place and removed (A1 anchor, $e_n/L_p = 0.15$).

the soil. Anchor rotation is governed by the moment acting at the centroid of the anchor, which itself is governed by the eccentricity of the padeye and the inclination of the mooring line. The inclination of the mooring line is also influenced by the anchor rotation and displacement, with a higher likelihood of a lower inclination at the anchor padeye (lower $\theta_a$) as the anchor rotates and becomes shallower.

### 4.2. Effect of a higher padeye eccentricity

Prompted by the lack of anchor rotation in tests with Anchor A1 ($e_n/L_p = 0.15$), the focus in the centrifuge tests turned to the response of anchors with different padeye eccentricity ratios. Fig. 9 compares the capacity mobilisation response for the different padeye eccentricities and embedment depths when loaded through a catenary mooring ($\theta_m = 0°$). The embedment effect is clear, with $F_u$ increasing by between 39% and 96% as $H_{tip}/L_p$ increases from 2 to 3. Fig. 9 also shows the effect due to padeye eccentricity, with increases in $F_u$ of 73% at $H_{tip}/L_p = 2$ and 100% at $H_{tip}/L_p = 3$ as $e_n/L_p$ increases from 0.15 to 1, although the increase appears to be non-linear with only a marginal increase in $F_u$ between $e_n/L_p = 0.6$ and $e_n/L_p = 1$. Images taken of repeat tests at $H_{tip}/L_p = 3$ that were stopped at approximately the ultimate capacity are provided in Fig. 10 and assist with understanding the effect of change in $e_n/L_p$. These images show (at the ultimate anchor capacity) that as $e_n/L_p$ increases from 0.15 to 1, anchor rotation increases from 0 to 16° ($\alpha_u = 90$ to 74°), the inclination of the mooring line at the anchor padeye increases from $\theta_a = 27.8$ to 53.2°, and the vertical embedment of the plate reduces from

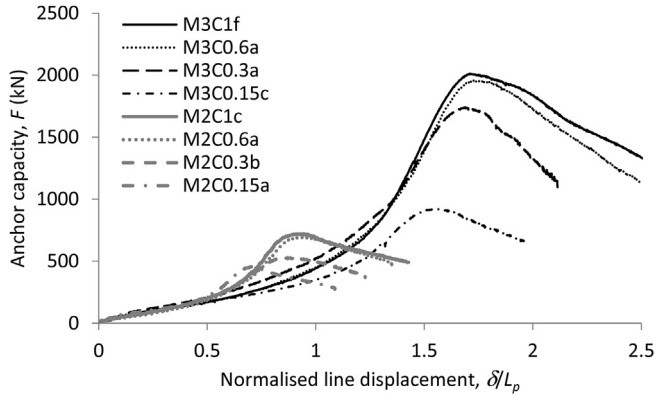


**Fig. 9.** Capacity mobilisation for anchors with different padeye eccentricities loaded through a catenary mooring.

$\Delta z/L_p = 0.83$ to $\Delta z/L_p = 0.38$. These effects are due to the magnitude of the moment generated at the centroid of the plate. At low $e_n/L_p$ the load in the initially vertical mooring line will result in a relatively low moment, meaning that it will be easier for the anchor to displace and for the mooring line to cut through the soil than for the anchor to rotate. In contrast, at high $e_n/L_p$ the mooring line load generates a greater moment, and an associated higher plate rotation. This anchor rotation has two effects. Firstly, it reduces the potential for the anchor to displace vertically – as also observed for plate anchors in clay (e.g. O'Loughlin et al., 2006) – which has the effect of increasing the capacity. Secondly, it reduces the potential for the mooring line to cut through the soil as the limiting mooring line inclination at the anchor padeye is normal to the plate, i.e. $\theta_a \geq 90 - \alpha_u$.

A more thorough consideration of the anchor capacity-kinematic response can be made by examining the anchor capacity and rotation (derived from the accelerometer measurements, Equation (2)) for anchor A4 ($e_n/L_p = 1$). The capacity and rotation response of Test M3C1g is shown on Fig. 11, together with post-testing images (from repeat tests) where loading was stopped before, at and after the ultimate anchor capacity. The response on Fig. 11 can be considered as three stages:

- Stage 1: the capacity mobilisation response is initially soft with very little anchor rotation ($\alpha < 87°$), which suggests that this stage is dominated by the mooring line cutting through the soil.
- Stage 2: the mooring line load tends to increase plate rotation rather than further cutting of the mooring line through the soil, eventuating in an ultimate capacity at an anchor rotation, $\alpha_u = 75.6°$ and a loss in anchor embedment, $\Delta z/L_p = 0.38$.
- Stage 3: anchor capacity and plate rotation reduces. Similar to observations made in Chow et al. (2015), the reduction in plate rotation is considered to be due to the mooring line reaching an inclination that causes the plate to rotate back towards it initial orientation (note point III in the post-testing images), with a capacity reduction that is considered to be due to the anchor becoming shallower.

The A4 anchor with the highest normalised padeye eccentricity ($e_n/L_p = 1$) was also loaded vertically at two embedment depths (Tests M2V1a and M3V1b). Fig. 12a shows the capacity mobilisation response together with the corresponding anchor rotation measurements for Test M2V1a at $H_{tip}/L_p = 2$. Three stages are apparent:

- Stage 1: Under vertical loading, the anchor is immediately loaded and the load-displacement response is initially stiff as the plate begins to rotate and develop capacity, before becoming softer at a rotation of around 77°, when the capacity starts to reduce.
- Stage 2: The capacity initially reduces (by about 20%) as the anchor rotates from 77° to 47°, before increasing towards a maximum capacity at a rotation of 14°. The magnitude of this ultimate capacity is approximately equal to that observed at the end of Stage 1. Load oscillations in the capacity curve are evident, particularly as the capacity maximises. Such oscillations are typical of those observed in vertical tensile loading tests of anchors and pipes in sand (e.g. Trautmann et al., 1985; Dickin, 1994; Cheuk et al., 2008; O'Loughlin and Barron, 2012) and are attributed to the progressive infilling of the void that forms behind the plate as the anchor displaces and rotates.
- Stage 3: The capacity reduces sharply despite continued plate rotation to the limiting value of 0°. This is consistent with observations reported by O'Loughlin and Barron (2012), which showed that the ultimate capacity can occur before the full bearing area of the plate is mobilised when the rotation is sufficient to trigger a transition from a deep to a shallow failure mechanism.

Fig. 12b shows that the response is somewhat similar when the embedment is higher ($H_{tip}/L_p = 3$, Test M3V1b), although unlike for the shallower case the ultimate capacity (i.e. at the end of Stage 2) is about 50% higher than the capacity at the end of Stage 1. This is due to the

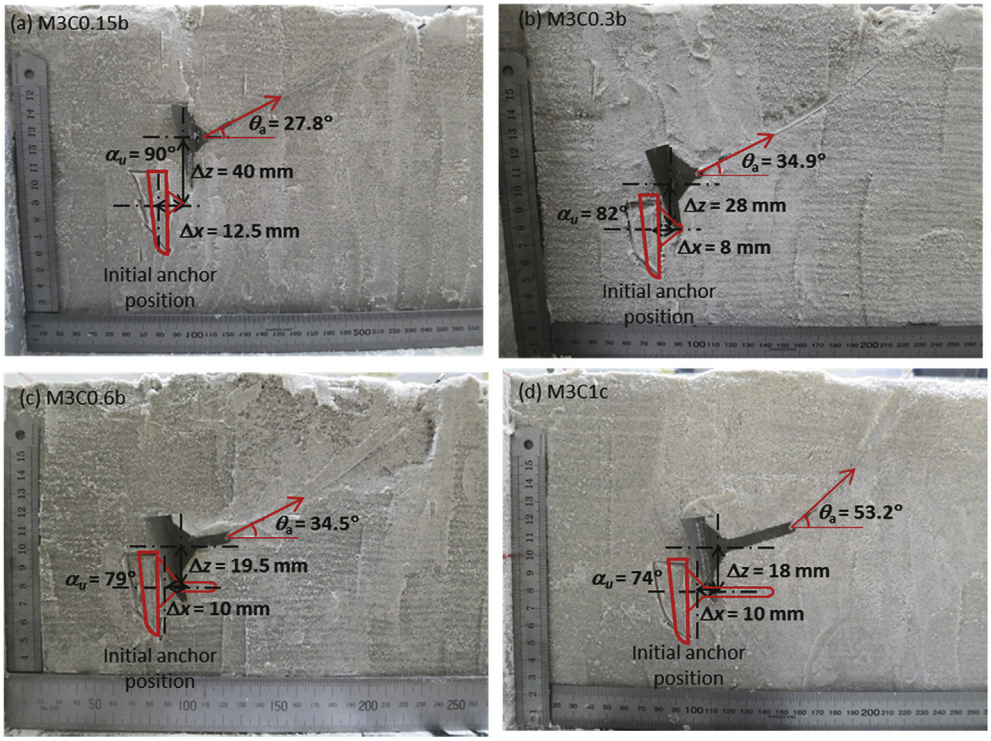


**Fig. 10.** Post-test visual examination at ultimate capacity for anchors with: (a) $e_n/L_p = 0.15$; (b) $e_n/L_p = 0.3$; (c) $e_n/L_p = 0.6$; (d) $e_n/L_p = 1$.

deeper embedment; i.e. examination of Fig. 12 reveals that the anchor embedment depth at ultimate capacity is approximately $L_p$ and $2L_p$ for Tests M2V1a and M3V1b, respectively. Although there were no anchor rotation measurements in this test, Fig. 12b also shows the capacity and rotation response for a vertically loaded strip anchor (Test M5V1, with a length to width ratio of 7) with $e_n/B = 1$ and $H/B = 5$ ($H_{tip}/B = 5.5$) in dense silica sand reported in O'Loughlin and Barron (2012). The capacity response is similar (noting that the comparison is facilitated by normalising the displacement by the plate width, $B$, for the strip anchor and by the plate height, $L_p$ for the anchor tests considered here), which suggests that the rotation response in Test M3V1b is likely to be similar to that of the strip anchor.

### 4.3. Anchor capacity factors

Experimentally determined anchor capacity factors, $N_\gamma$, from the monotonic tests are summarised in Fig. 13 and clearly show the dependence of capacity on embedment depth, load inclination and padeye eccentricity ratio. The dependence on padeye eccentricity is best demonstrated through the tests with $\theta_m = 0°$ (Fig. 13a). These data show a strong positive effect on anchor capacity up to $e_n/L_p = 0.6$, with increases in $N_\gamma$ of up to 56% and 108% at $H_{tip}/L_p = 2$ and 3 respectively, but negligible effects thereafter. The lower experimentally $N_\gamma$ at lower $e_n/L_p$ reflects the higher loss in embedment (as $N_\gamma$ is calculated using the initial embedment depth, $H$, and not the reduced embedment depth at the ultimate capacity) and the reduced plate rotation (and hence projection of the plate towards the loading direction). Similar effects of padeye eccentricity on keying-induced loss in embedment (and hence potential anchor capacity) have been observed in both clay (e.g. O'Loughlin et al., 2006; Gaudin et al., 2009) and sand (Barron, 2014). Fig. 13 also shows the strong effects due to embedment depth and mudline load inclination. For instance, for an anchor with $e_n/L_p = 1$, capacity increases by 427% from $N_\gamma = 2.6$ at $H_{tip}/L_p = 2$ and for $\theta_m = 90°$ (Fig. 13b), to (a maximum) $N_\gamma = 13.7$ at $H_{tip}/L_p = 3$ and for $\theta_m = 0°$ (Fig. 13a). This increase in $N_\gamma$ with increasing embedment depth and reducing mudline load inclination is due to the extent of the failure mechanism, which increases as the load direction becomes more horizontal and as the embedment depth increases (e.g. see Merifield and Sloan, 2006).

Also shown on Fig. 13b are the numerical solutions for horizontal plate anchors in sand under vertical loading reported by Merifield and Sloan (2006) and Merifield et al. (2006), which serve as comparisons to the centrifuge data for vertical loading, noting that at high $e_n/L_p$ the anchor approached a near horizontal orientation at ultimate capacity. The solutions on Fig. 13b are provided for a friction angle, $\phi = 37°$, as appropriate for the relative density and stress levels in these centrifuge tests (Bolton, 1987). Although the aspect ratio, $L_p/W = 1.33$ (i.e. close to a square), the plate width tapers towards the anchor tip, such that the equivalent aspect ratio near the tip is closer to 3.5. For this reason, and given the complex geometry of the plate anchor, solutions for both strip and square anchors are provided. Experimentally determined values of $N_\gamma$ lie between the solutions for the strip and square at $e_n/L_p = 1$, but lie beneath both solutions at $e_n/L_p = 0.15$. Although Merifield and Sloan (2006) also provide solutions for horizontally loaded vertical plate anchors (i.e. a horizontal load applied to the padeye of a vertical plate anchor), there are no existing theoretical or numerical solutions relevant to the more realistic scenario offshore (and modelled in these centrifuge tests), where the load is horizontal at the mudline and consequently inclined at the padeye.

## 5. Results: cyclic capacity

As outlined earlier in the paper, the cyclic tests considered the A4 anchor with $e_n/L_p = 1$ at a fixed embedment ratio, $H_{tip}/L_p = 2$ and load inclination at the mudline, $\theta_m = 0°$. The loading sequences for both the regular and irregular cyclic loading are shown in Fig. 14. A slack mooring was modelled using a nominal mooring line load (CLR = 0.05 in the regular cyclic loading tests and 20 N in the irregular cyclic loading tests) to avoid issues with the load control algorithm trying to achieve 0 N. Key results from the cyclic tests and the equivalent monotonic test are summarised in Table 2.

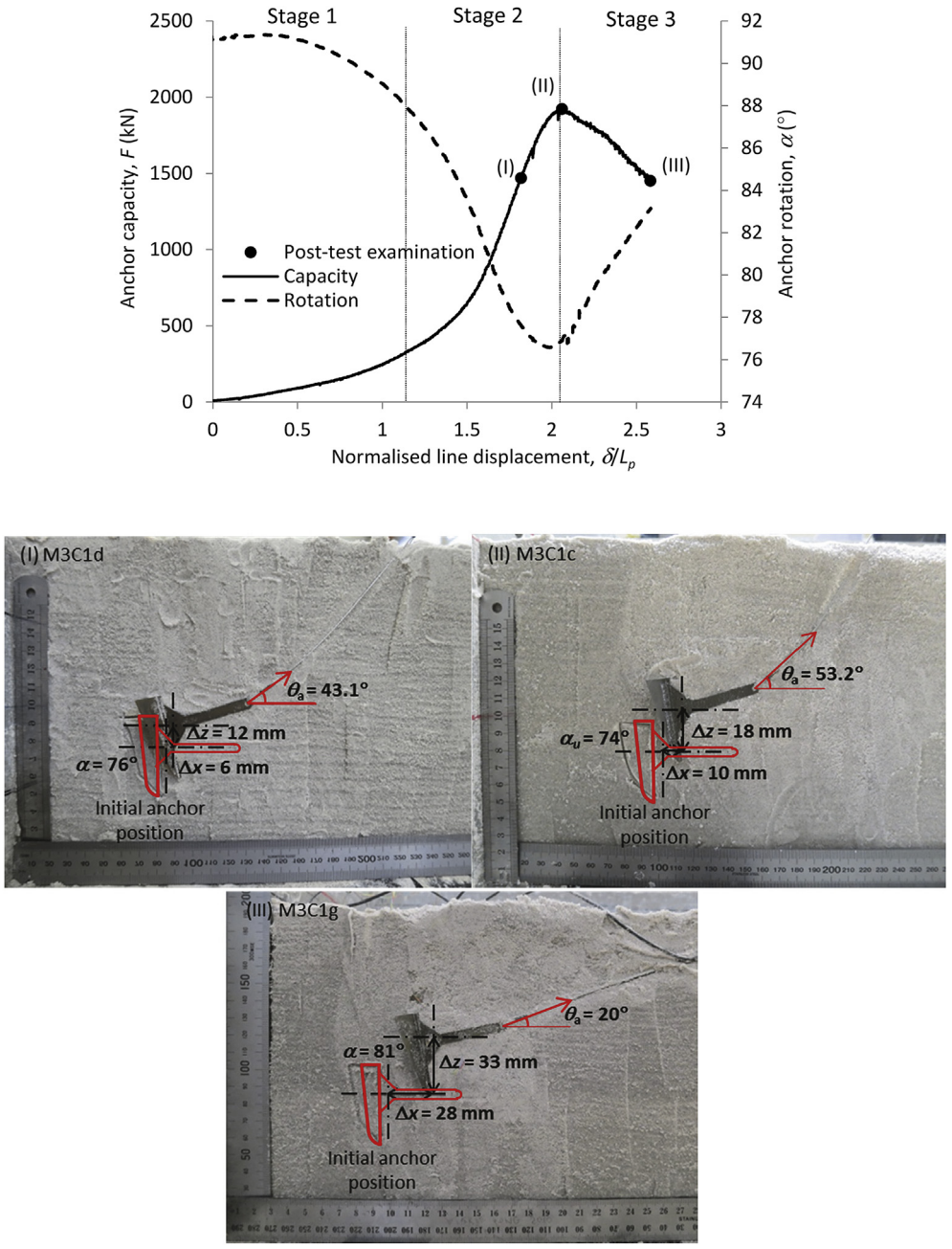


**Fig. 11.** Anchor capacity and rotation response in Test M3C1g ($e_n/L_p = 1$, $\theta_m = 0°$, $H_{tip}/L_p = 3$).

### 5.1. Regular cyclic loading

As shown in Fig. 14a, the regular cyclic loading involved a sinusoidal wave with a fixed minimum load (CLR = 0.05) but with an increasing amplitude (starting at a maximum load of CLR = 0.2) that was maintained for 'packets' of 300 cycles, before being stepped to the next amplitude at a fixed CLR increment of 0.10 until failure occurred.

Fig. 15 compares the results from the two repeat cyclic tests with the equivalent monotonic test. The initial loading to 70% of the monotonic anchor capacity is identical, but the subsequent cyclic loading is seen to lead to improvements in the anchor capacity, with an average ultimate capacity, $F_u$ = 1002.8 kN ($N_\gamma$ = 11.6), that is 28.8% higher than the monotonic ultimate capacity ($F_u$ = 780 kN, $N_\gamma$ = 9). A third cyclic test was conducted but stopped when the CLR reached 0.7 to permit a visual comparison with the corresponding monotonic test that was also stopped at 70% of the monotonic anchor capacity (Test RC2C1c). The comparison is provided in Fig. 16, which shows consistent anchor and mooring line inclinations between the two tests (differing by 0.5° for the anchor and 1.2° for the mooring line), but significantly lower loss in embedment for the cyclically loaded anchor ($\Delta z/L_p$ = 0.08 compared to $\Delta z/L_p$ = 0.31), which explains the higher ultimate cyclic capacity.

### 5.2. Irregular cyclic loading

The irregular cyclic loading tests involved a pre-programmed 'storm' of irregular cyclic loads (Fig. 14b and c) established from wave tank tests on a wave energy converter with catenary moorings (Casaubieilh et al., 2014). Two irregular cyclic loading tests were conducted using the storm shown on Fig. 14b and c, but with both the storm duration and the peak cyclic load scaled. Test IC2C1a1 involved 15 storms with the peak cyclic load equal to the monotonic anchor capacity ($CLR_{peak}$ = 1), whereas Test IC2C1a1.5 involved a single storm in which the peak cyclic load was 50%

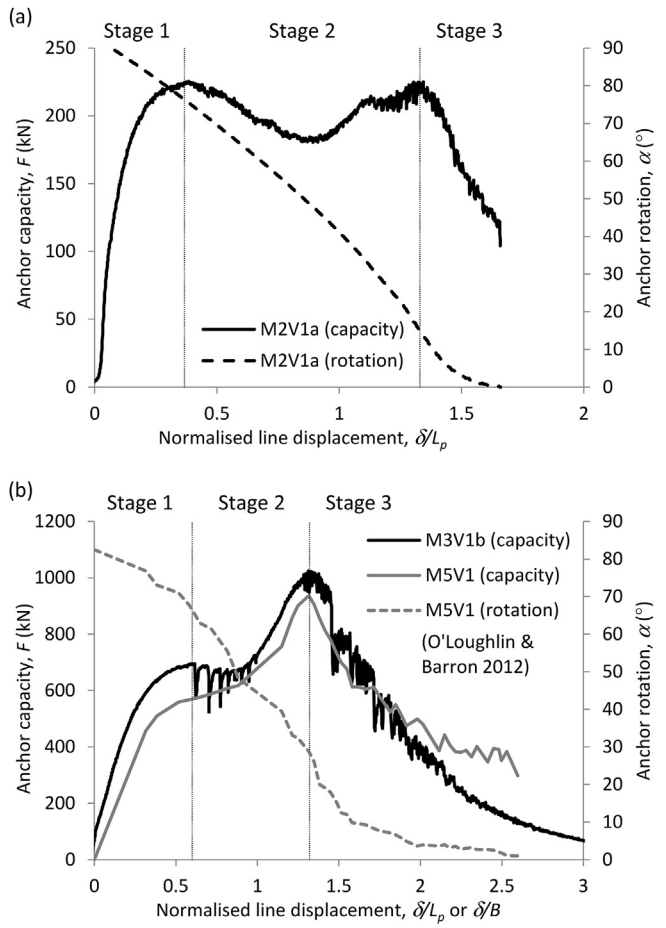


**Fig. 12.** Mobilisation of anchor capacity and anchor rotation response for a vertically loaded anchor with $e_n/L_p = 1$ at: (a) $H_{tip}/L_p = 2$ and (b) $H_{tip}/L_p = 3$ (including data from O'Loughlin and Barron (2012) for a vertically loaded strip anchor).

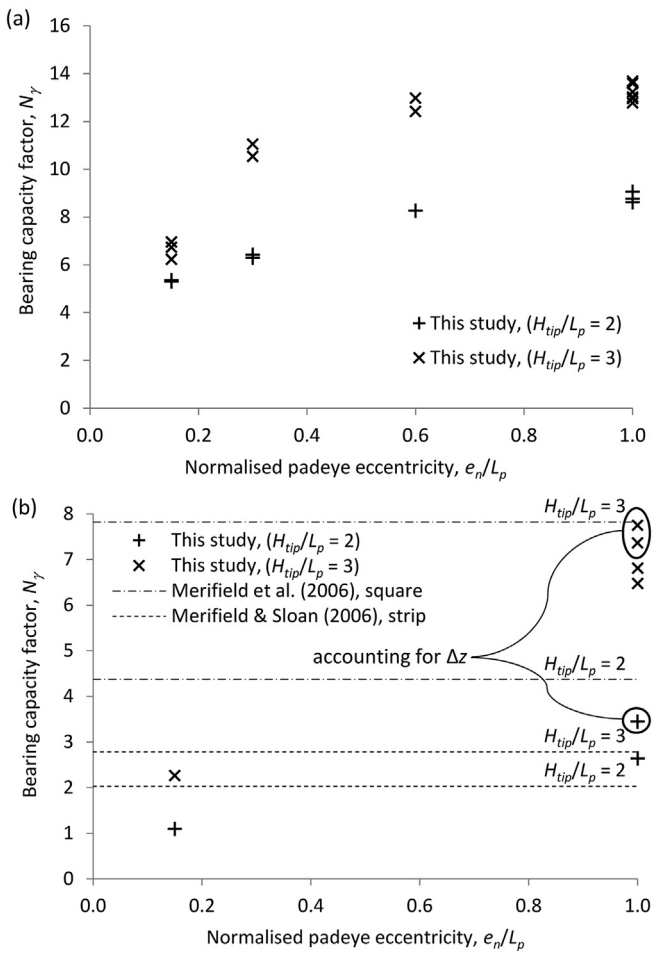


**Fig. 13.** Anchor capacity factors: (a) catenary mooring ($\theta_m = 0°$); (b) taut (vertical) mooring ($\theta_m = 90°$).

higher than the monotonic anchor capacity (i.e. $CLR_{peak} = 1.5$).

The irregular cyclic loading test results are compared with the equivalent monotonic test in Fig. 17, where it can be seen that the anchor was capable of withstanding 15 storms at $CLR_{peak} = 1$, but not a single storm with $CLR_{peak} = 1.5$. The post-cyclic monotonic test following the 15 storms resulted in an eventual anchor capacity, $F_u = 1030.0$ kN ($N_\gamma = 12.3$), 43% higher than the reference monotonic ultimate capacity, $F_u = 721.2$ kN ($N_\gamma = 8.6$). Failure occurred quickly in Test IC2C1a1.5, with significant mooring line displacement at a CLR = 1.17, with an observed cyclic ultimate capacity, $F_u = 863.4$ kN ($N_\gamma = 10.2$), 20% higher than the reference monotonic ultimate capacity. Fig. 17b shows that the rotation response of the anchor is similar, albeit with some minor differences in rotation at the peak capacity.

The higher drained anchor capacity measured during or after cyclic loading is consistent with other plate anchor studies involving drained cyclic loading (e.g. Chow et al., 2015) and also the response of piles due to drained cyclic loading in sand (e.g. Nicolai et al., 2017). Relatively low magnitude cyclic loading (such as in Test IC2C1a1) allows for densification that improves anchor capacity, whereas the more onerous cyclic loading in Test IC2C1a1.5 involved load cycles that approached the anchor capacity before significant densification, such that the higher peak cyclic loads could not be tolerated. Such behaviour can be captured by kinematic hardening soil models that account for stress history (e.g. Corti et al., 2016).

## 6. Conclusions

This paper considers the drained capacity of a dynamically installed plate anchor in dense sand under monotonic and cyclic loading. The blade-like anchor design was prompted by a requirement to minimise penetration resistance during dynamic installation, which resulted in an anchor padeye that was located close to the plate. However, the centrifuge data considered in this paper reveal that the low padeye eccentricity is problematic for mobilising anchor capacity, as there is insufficient lever arm to develop the moment loading that will initiate anchor rotation and subsequently develop the highest bearing resistance on the anchor plate. A more optimal anchor design would be to employ a padeye eccentricity equal to about 0.6 times the plate height. Consideration would need to be given to the influence of an eccentric padeye during dynamic installation as this may affect both the verticality of the anchor during free-fall and the potential to achieve adequate penetration. In this respect a bridle arrangement or a rotating padeye arm may be a practical solution that would allow the padeye to be located parallel and close to the plate during installation, and eccentric from the plate during loading.

The centrifuge tests involved jacked installation to an anchor tip embedment that was either two or three times the plate height, as the dynamic installation centrifuge tests reported in Chow et al. (2017) indicate that this level of embedment is achievable. The test data show that the plate anchor is most efficient in sand when loaded through a catenary rather than a vertical mooring. This is partly due to the anchor kinematics, as (for a high padeye eccentricity) a vertical mooring causes significant anchor rotation and loss of embedment, whereas a catenary mooring leads to much more moderate rotation and embedment loss. A catenary mooring is also more efficient as the loading at the padeye is inclined rather than vertical, such that the failure mechanism is likely to involve a much larger soil mass.

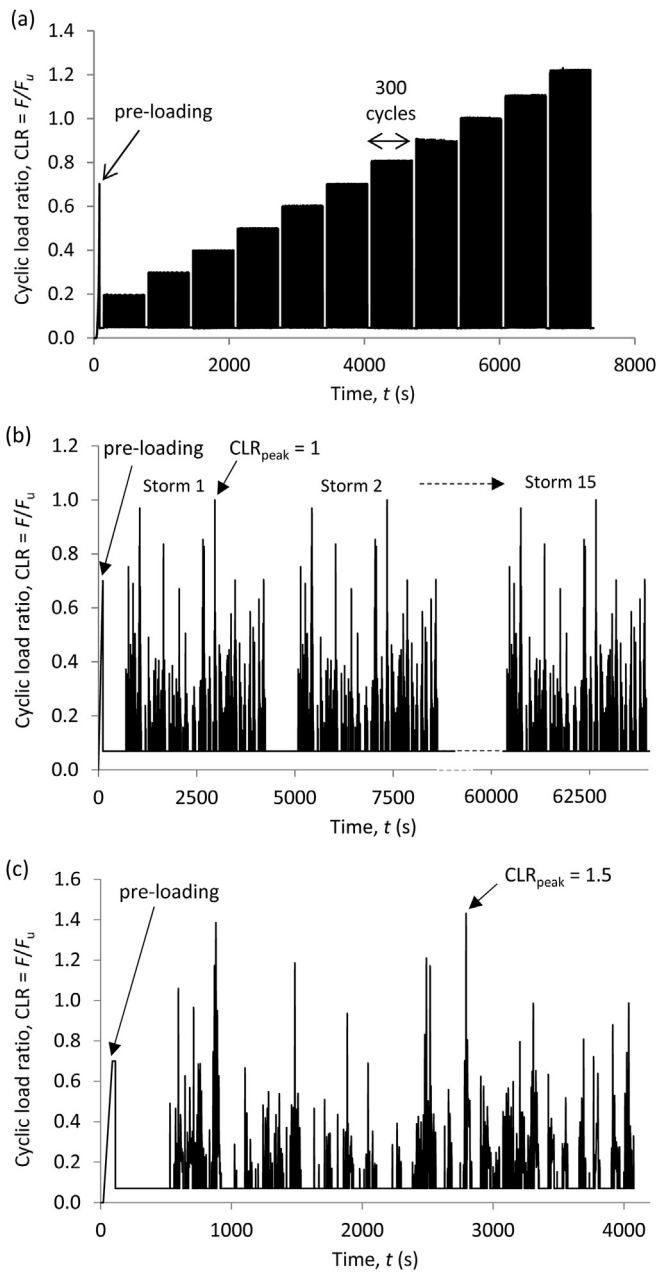


**Fig. 14.** Cyclic loading sequence: (a) regular cyclic loading; (b) irregular cyclic loading (Test IC2C1a1); (c) irregular cyclic loading (Test IC2C1a1.5).

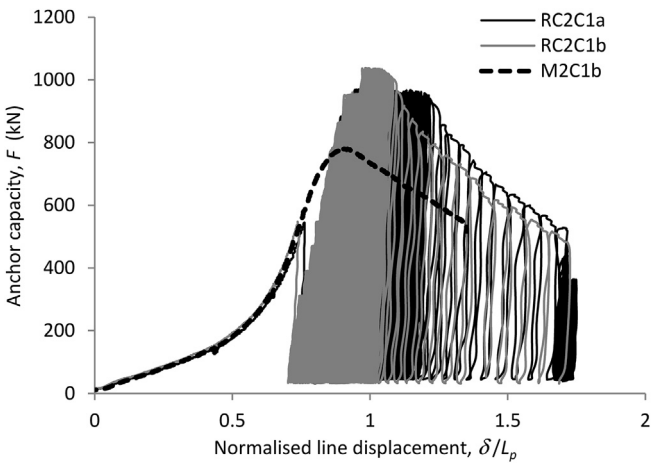


**Fig. 15.** Increase in anchor capacity due to regular cyclic loading.

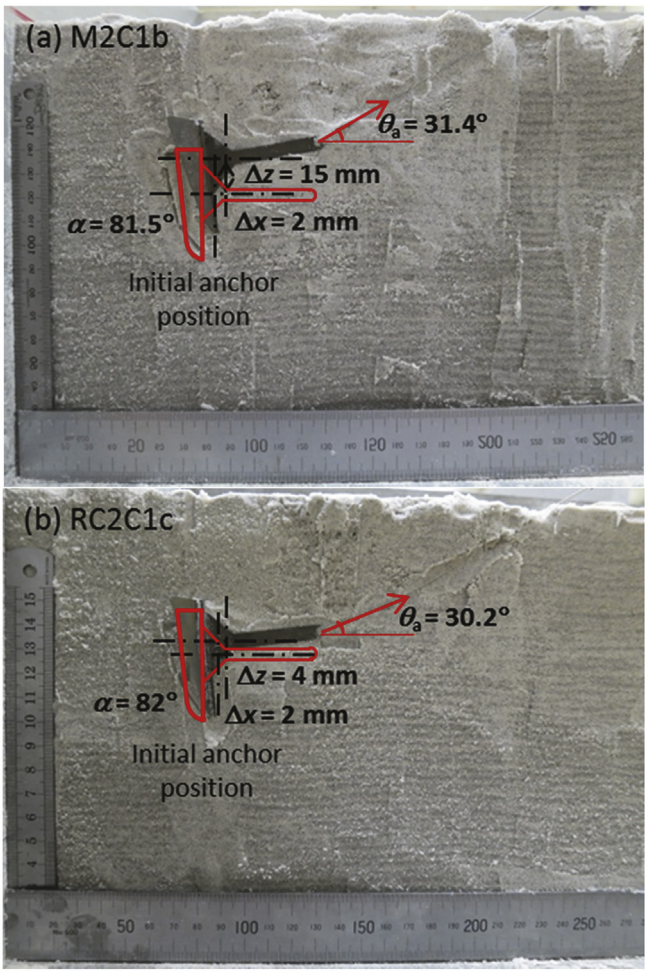


**Fig. 16.** Comparison of anchor and mooring line position and orientation prior to mobilisation of peak capacity: (a) monotonic loading; (b) regular cyclic loading.

The centrifuge test data indicate that an anchor capacity factor, $N_\gamma = 13$ is achievable, with an equivalent anchor capacity of approximately 2 MN for the 2.4 m high prototype plate anchor considered here. In the context of mooring line loads for marine renewable energy devices, Azcona et al. (2017) calculate a maximum dynamic mooring line load of approximately 3 MN for a 5 MN offshore wind turbine stabilised by a spar platform, whereas Palm et al. (2013) calculate a maximum dynamic mooring line load of approximately 550 kN for a wave energy converter that was modelled as a cylinder with a mass of 100 tonnes. Hence the prototype equivalence of the anchor considered in the centrifuge tests would require moderate upscaling for the wind turbine, but significant downscaling for the wave energy converter.

Comparisons with existing theoretical and numerical solutions for anchor capacity in sand is hampered by the limiting and unrealistic assumptions regarding load direction and plate inclination, which are unrealistic for offshore anchors that are installed vertically. The centrifuge data show that drained cyclic loading improves anchor capacity by up to 43%, with lower level cyclic loading leading to the greatest gains. The effect of partially drained cyclic loading is unclear, and warrants further attention given the dynamic nature of cyclic loading on offshore renewable energy devices, including the potential for high magnitude

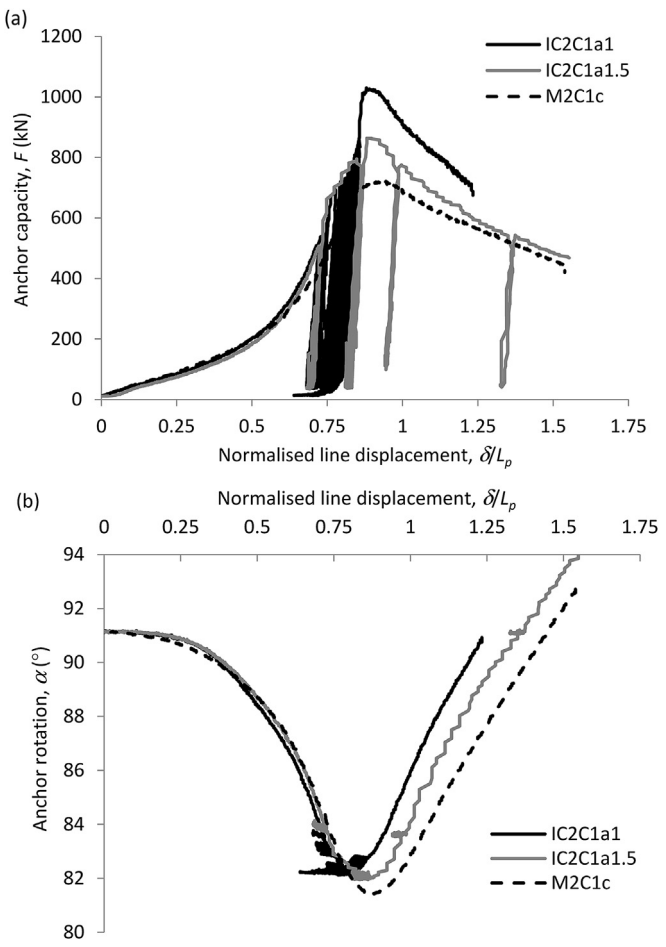


**Fig. 17.** Capacity mobilisation and anchor rotation due to monotonic and irregular cyclic loading ($e_n/L_p = 1$, $H_{tip}/L_p = 2$).

short duration 'snap' or 'snatch' loads (e.g. Hann et al., 2015; Hsu et al., 2017).

## Acknowledgements

This work forms part of the activities of the Centre for Offshore Foundation Systems (COFS), currently supported as a node of the Australian Research Council Centre of Excellence for Geotechnical Science and Engineering and as a Centre of Excellence by the Lloyd's Register Foundation. The Lloyd's Register Foundation invests in science, engineering and technology for public benefit, worldwide. The research leading to these results has received funding from the European Union Seventh Framework Programme (FP7/2007–2013) under grant agreement no. 287056.

## References

Azcona, J., Palacio, D., Munduate, X., González, L., Nygaard, T.A., 2017. Impact of mooring lines dynamics on the fatigue and ultimate loads of three offshore floating wind turbines computed with IEC 61400-3 guideline. Wind Energy 20, 797–813.
Barron, B., 2014. An Investigation into the Keying Behaviour and the Capacity of Plate Anchors. MEng Thesis. Institute of Technology, Sligo.
Bolton, M.D., 1987. Discussion: the strength and dilatancy of sands. Geotechnique 37 (2), 219–226.
Casaubieilh, P., Thiebaut, F., Bosma, B., Retzler, C., Shaw, M., Letertre, Y., Sheng, W., 2014. Performance improvements of mooring systems for wave energy converters. In: Proc. 1st Renewable Energies Offshore, RENEW 2014, Lisbon, Portugal.
Cheuk, C., White, D., Bolton, M., 2008. Uplift mechanisms of pipes buried in sand. J. Geotech. Geoenviron. Eng. 134 (2), 154–163.
Chow, S.H., O'Loughlin, C.D., Corti, R., Gaudin, C., Diambra, A., 2015. Drained cyclic capacity of plate anchors in dense sand : experimental and theoretical observations. Géotech. Lett. 5, 80–85.
Chow, S.H., O'Loughlin, C.D., Gaudin, C., Knappett, J.A., Brown, M.J., Lieng, J.T., 2017. An experimental study of the embedment of a dynamically installed anchor in sand. In: Proceedings of the 8th Offshore Site Investigation and Geotechnics Conference (OSIG17), London, UK, pp. 1019–1025.
Corti, R., Diambra, A., Muir Wood, D., Escribano, D.E., 2016. Memory surface hardening model for granular soils under repeated loading conditions. J. Eng. Mech. 142 (12), 04016102.
Diaz, B.D., Rasulo, M., Aubeny, C.P., Fontana, C.M., Arwade, S.R., Degroot, D.J., Landon, M., 2016. Multiline anchors for floating offshore wind towers. In: OCEANS 2016 MTS/IEEE Monterey, OCE 2016. https://doi.org/10.1109/OCEANS.2016.7761374.
Dickin, E.A., 1994. Uplift resistance of buried pipelines in sand. Soils Found. 34, 41–48.
Gaudin, C., Tham, K., Ouahsine, S., 2009. Keying of plate anchors in NC clay under inclined loading. Int. J. Offshore Polar Eng. 19 (2), 135–142.
Gaudin, C., O'Loughlin, C.D., Duong, M.T., Herduin, M., Fiumana, N., Draper, S., Wolgamot, H., Zhao, L., Cassidy, M.J., 2017. New anchoring paradigms for floating renewables. In: Proceedings of the 12th European Wave and Tidal Energy Conference, Cork, Ireland.
Garnier, J., Gaudin, C., Springman, S.M., Culligan, P.J., Goodings, D., Konig, D., Randolph, M.F., Thorel, L., 2007. Catalogue of scaling laws and similitude questions in geotechnical centrifuge modelling. Int. J. Phys. Model. Geotech. 7 (3), 1–23.
Gerkus, H.S., Giampa, J.R., Senanayake, A.I., Lai, Y., Huang, Y., Flores, J.E.I., Breithaupt, B., Sivarajah, S., Bradshaw, A.S., Gilbert, R.B., 2016. Preliminary development of a new concept to improve sustainability of offshore foundations. In: Geo-Chicago 2016 Conference, pp. 459–469.
Hann, M., Greaves, D., Raby, A., 2015. Snatch loading of a single taut moored floating wave energy converter due to focussed wave groups. Ocean. Eng. 96, 258–327.
Heurlin, K., Rességuier, S., Melin, D., Nilsen, K.R., 2015. Comparison between FEM analyses and full-scale tests of fluke anchor behavior in silty sand. In: Proc. International Symposium on Frontiers in Offshore Geotechnics, Oslo, Norway, 875–880.
Hsu, W., Thiagarajan, K., Manuel, L., 2017. Extreme mooring tensions due to snap loads on a floating offshore wind turbine system. Mar. Struct. 55, 182–199.
Knappett, J.A., Brown, M.J., Aldaikh, H., Patra, S., O'Loughlin, C.D., Chow, S.H., Gaudin, C., Lieng, J.T., 2015. A review of anchor technology for floating renewable energy devices and key design considerations. In: Proc. 3rd International Symposium on Frontiers in Offshore Geotechnics, Oslo, Norway, pp. 887–892.
Lieng, J.T., Kavli, A., Hove, F., Tjelta, T.I., 2000. Deep penetrating anchor: further development, optimization and capacity verification. In: Proc. 10th International Offshore and Polar Engineering Conference, Seattle, Washington, pp. 410–416.
Medeiros Jr., C.J., 2002. Low cost anchor system for flexible risers in deep waters. In: Proc. Offshore Technology Conference, Houston, Texas, p. 14151.
Merifield, R., Sloan, S., 2006. The ultimate pullout capacity of anchors in frictional soils. Can. Geotech. J. 43, 852–868.
Merifield, R., Sloan, S., Lyamin, A., 2006. Three dimensional lower bound solutions for the stability of plate anchors in sand. Geotechnique 56 (2), 123–132.
Neubecker, S.R., Randolph, M.F., 1996. The kinematic behaviour of drag anchors in sand. Can. Geotech. J. 33 (4), 584–594.
Nicolai, G., Ibsen, L.B., O'Loughlin, C.D., White, D.J., 2017. Quantifying the increase in lateral capacity of monopiles in sand due to cyclic loading. Géotech. Lett. 7 (3), 245–252.
O'Loughlin, C.D., Barron, B., 2012. Capacity and keying response of plate anchors in sand. In: Proc. 7th International Conference Offshore Site Investigation and Geotechnics, pp. 649–655.
O'Loughlin, C.D., Randolph, M.F., Richardson, M.D., 2004. Experimental and theoretical studies of deep penetrating anchors. In: Offshore Technology Conference. Houston, Texas, p. 16841.
O'Loughlin, C.D., Lowmass, A., Gaudin, C., Randolph, M.F., 2006. Physical modelling to assess keying characteristics of plate anchors. In: Proc. 6th Physical Modelling in Geotechnics, pp. 659–666.
O'Loughlin, C.D., Blake, A.P., Richardson, M.D., Randolph, M.F., Gaudin, C., 2014. Installation and capacity of dynamically embedded plate anchors as assessed through centrifuge tests. Ocean. Eng. 88, 204–213.
O'Loughlin, C.D., Neubecker, S.R., Gaudin, C., 2017. Anchoring Systems: Anchor Types, Installation and Design. Encyclopaedia of Marine and Offshore Engineering, Wiley accepted.
Palm, J., Eskilsson, C., Moura Paredes, G., Bergdahl, L., 2013. CFD Simulation of a moored floating wave energy converter. In: 10th European Wave and Tidal Energy Conference.
Shelton, J.T., 2007. OMNI-maxtrade anchor development and technology. In: Proc. OCEANS Conference, Vancouver, pp. 1–10.
Silva, M.F., Bolton, M.D., 2004. Centrifuge penetration tests in saturated layered sands. In: Proc. 2nd International Conference on Site Characterization, Porto, pp. 377–384.
Tian, Y., Randolph, M.F., Cassidy, M.J., 2015. Analytical solution for ultimate embedment depth and potential holding capacity of plate anchors. Geotechnique 65 (6), 517–530.
Trautmann, C.H., O'Rourke, T.D., Kulhawy, F.H., 1985. Uplift force-displacement response of buried pipe. J. Geotech. Eng. 111, 1061–1076.

## Notation

$\alpha$: anchor rotation angle

$\alpha_u$: anchor rotation angle at ultimate capacity
$\gamma'$: effective unit weight
$\phi$: friction angle
$\phi'_{cs}$: critical state friction angle
$\theta_a$: mooring line angle at padeye (to the horizontal)
$\theta_m$: load inclination at mudline (to the horizontal)
$\rho_d$: dry density
$\rho_{max}$: maximum dry density
$\rho_{min}$: minimum dry density
$\rho_{sat}$: saturated density
$\delta_u$: line displacement at ultimate capacity
$\Delta x$: horizontal movement of anchor
$\Delta z$: vertical movement or loss in embedment of anchor
$\Delta z/L_p$: normalised loss in embedment
$A_p$: projected area of the anchor plate
$A_x$: acceleration in the x-axis (parallel to the plate)
$A_y$: acceleration in the y-axis (normal to the plate)
$B$: width of a rectangular plate anchor
*CLR:* cyclic load ratio (ratio of cyclic load to monotonic ultimate capacity)
$CLR_{peak}$: peak cyclic load ratio (ratio of peak cyclic load to monotonic ultimate capacity)
$d_{10}$, $d_{50}$, $d_{60}$: sand particle size at 10%, 50% and 60% passing respectively
$D_r$: relative density
$e_n$: padeye eccentricity normal to the anchor
$e_n/L_p$: normalised padeye eccentricity (normal to anchor)
$f$: frequency
$F$: anchor capacity
$F_u$: ultimate anchor capacity
*Gs:* specific gravity
$H$: initial depth to the anchor padeye and centroid
$H_{tip}$: depth to the anchor tip
$H/B$: normalised initial depth ratio measured to the anchor centroid (for a rectangular plate anchor with width, $B$)
$H/L_p$: normalised initial depth ratio measured to the anchor padeye and centroid
$H_{tip}/L_p$: normalised depth ratio measured to the anchor tip
$L/B$: aspect ratio of a rectangular plate anchor with length, $L$ and width, $B$
$L_p$: length of plate anchor
$L_p/W$: aspect ratio of plate anchor
$L_f$: follower length
$m$: plate anchor mass
*MEMS:* Micro-electro mechanical system
$N_\gamma$: anchor capacity factor
$q_c$: cone tip resistance
$t$: plate anchor thickness
*UWA:* University of Western Australia
$v$: actuator velocity
$W$: plate anchor width